Can. J. Remote Sensing, Vol. 31, No. 4, pp. 289–303, 2005

RADARSAT-1 images in support of petroleum exploration: the offshore Amazon River mouth example

R. Almeida-Filho, F.P. Miranda, J.A. Lorenzzetti, E.C. Pedroso, C.H. Beisl, L. Landau,
M.C. Baptista, and E.G. Camargo

Abstract: RADARSAT-1 images were used as an attempt to identify seepage slicks in the Foz do Amazonas Basin, one of the most promising oil and gas exploration frontiers in the Brazilian equatorial margin, a region that is cloud-covered for most of the year. An unsupervised semivariogram textural classifier algorithm was used to enhance areas of smooth texture and low radar backscatter, indicative of these seepage slick targets. Complementary information related to sea surface temperature, cloud top temperature, wind velocity, and modelling for the tidal regime (all obtained as close as possible to the RADARSAT-1 acquisition) was used to support image interpretation and to exclude false targets also characterized by low radar backscatter (e.g., local upwelling, heavy rain cells). Twenty-one target areas were interpreted as seepage slicks. Considering the influence of the oceanographic and environmental conditions on drifting of the interpreted seepage slicks, they were spatially compared with available geological information, including seismically derived structural and isopach maps, and bathymetric data. Most of the interpreted seepage slicks occur in an extensional structural domain of growth faults. These structures are related to Cenozoic gravity tectonics that result from tensional stress in the continental slope due to the huge load of fluvial sediments transported by the Amazon River. Together with previously discovered subcommercial shallow water oil accumulations, the remote detection of seepage slicks is additional evidence of present-day generation and migration phenomena. The results indicate that the use of a remote, swift method to identify offshore natural oil seepage related to active petroleum systems may constitute a well-accepted approach to support exploration in frontier areas like the Foz do Amazonas Basin.

Résumé : Des images RADARSAT-1 ont été utilisées dans une tentative d'identification des nappes de pétrole de suintement dans le bassin de Foz do Amazonas, une des zones éloignées les plus prometteuses en terme d'exploration pétrolière et gazière dans la marge équatoriale brésilienne, une région recouverte de nuages durant presque toute l'année. Nous avons appliqué un algorithme basé sur un classificateur de texture utilisant la technique du semi-variogramme non dirigé pour rehausser les zones de texture fine et de faible rétrodiffusion radar qui sont des indicateurs de ces cibles. Des informations complémentaires reliées à la température de la surface de la mer, à la température au sommet des nuages, à la vitesse du vent et à la modélisation du régime des marées (toutes obtenues le plus près possible du moment de l'acquisition RADARSAT-1) ont été utilisées comme outil pour l'interprétation des images et pour exclure les fausses cibles caractérisées elles aussi par une rétrodiffusion radar faible (i.e., résurgence locale, cellules de fortes averses). Vingt-et-une zones cibles ont été interprétées comme étant des nappes de suintement. Considérant l'influence des conditions océanographiques et environnementales sur la dérive des nappes de suintement interprétées, celles-ci ont été comparées spatialement aux informations géologiques disponibles, incluant les cartes structurales et d'isopaques dérivées par sismographie et les données bathymétriques. La plupart des nappes de suintement interprétées se situent dans le domaine structural étendu des failles de croissance. Ces structures sont reliées à la tectonique de gravité Cénozoïque résultant du stress à la surface de la pente continentale dû à l'énorme charge de sédiments fluviatiles transportée par le fleuve Amazone. Parallèlement aux accumulations de pétrole à valeur commerciale faible découvertes en eau peu profonde antérieurement, la télédétection des nappes de suintement constitue une preuve additionnelle des phénomènes actuels de génération et de migration. Les résultats indiquent que l'utilisation d'une méthode à distance et rapide pour l'identification des fuites naturelles de pétrole au large reliées à des systèmes pétrolifères actifs peut constituer une approche qui serait favorablement accueillie dans le domaine de l'exploration en zones éloignées comme celle du bassin de Foz do Amazonas.
[Traduit par la Rédaction]

Received 28 April 2004. Accepted 11 April 2005.

R. Almeida-Filho,[1] J.A. Lorenzzetti, and E.G. Camargo. Instituto Nacional de Pesquisas Espaciais (INPE), CP 515, São José dos Campos SP, Brazil.

F.P. Miranda. Petrobras-CENPES, Ilha do Fundão, Q-7, Rio de Janeiro RJ, Brazil.

E.C. Pedroso and C.H. Beisl. CBRR-Coppe/UFRJ, CP 68552, Rio de Janeiro RJ, Brazil.

L. Landau and M.C. Baptista. Coppe/UFRJ, CP 68552, Rio de Janeiro RJ, Brazil.

[1] Corresponding author (e-mail: rai@ltid.inpe.br).

Introduction

The hydrocarbon industry is now focused on two main strategies: improving the capacity of recovering as much oil as possible from the existing fields, and exploring the last remaining frontier areas in the continental margins (White et al., 2003). With drilling in deep and ultra-deep water costing tens of millions of US dollars, there is an increasing need to bring together the skills of a number of experts in different fields, such as oceanography, meteorology, geochemistry, geophysics, and engineering, to contribute with new datasets and insights to decrease the risks in offshore exploration (Stankiewicz, 2003).

The use of information derived from modern remote sensing satellites can be one of these new sources of information, shedding light on oil frontier exploration areas. Recent studies (e.g., Estes et al., 1985; MacDonald et al., 1993; 1996; Miranda et al., 1998) have shown the feasibility of using orbital images (in either the visible or the microwave portions of the electromagnetic spectrum) to detect seepage slicks, therefore contributing to this modern offshore oil rush.

Images provided by the RADARSAT-1 satellite are suitable for this kind of application. In addition to penetrating clouds and haze, the sensitivity to small-scale surface roughness of C-band radar and the broad range of side-looking viewing geometries make RADARSAT-1 images ideal for offshore oil detection (Miranda et al., 2004).

Although natural oil seepage may originate from either commercial or noncommercial oil accumulations, the identification of such features is important because they constitute a direct indication of the presence of active petroleum systems, therefore increasing the exploratory potential of frontier exploration areas.

The aim of this study is to use information derived from the analysis of RADARSAT-1 images, combined with a broad range of ancillary data, to assess oil seepage phenomena in an exploration frontier offshore from the Amazon River mouth in the Brazilian equatorial margin. According to the three-level classification (high, moderate, and low) of the continental margins proposed by Wilson et al. (1974), the study area has a moderate potential for the occurrence of natural oil slicks.

Detection of seepage slicks using radar images depends on several factors such as the radar frequency, incidence angle, spatial resolution, environmental conditions, and size of the oil slicks. Since RADARSAT-1 images acquired under steep incidence angles are more favourable for the detection of seepage slicks, the wide 1 (W1) and ScanSAR narrow 1 (SCN1) beam modes were used in this study. The success of remote detection of seepage slicks is strongly dependent, however, on the meteorological and oceanographic conditions prevailing at the time of the synthetic aperture radar (SAR) image acquisition.

Capillary waves produced by wind on the sea surface cause diffuse backscatter of the C-band radar incident pulse. These waves, due to the damping phenomenon (Alpers and Hühnerfuss, 1989), can be inhibited by the presence of surface films of oil. As a result, areas containing oil appear darker in radar images than areas of adjoining sea clutter. Very weak winds do not produce enough sea clutter in the areas surrounding the seepage slick to give the necessary backscatter contrast to observe such a feature. Conversely, very strong winds can produce too much turbulence or waves, hindering detection. Wind speed values considered ideal for the remote detection of oil slicks range from 3 to 8 $m \cdot s^{-1}$ (Staples and Hodgins, 1998). Local upwellings, wind shadows, and biological surfactants are factors that could also cause a decrease in the radar backscatter (Fingas and Brown, 1997) and may be misinterpreted as associated with seepage slicks. Cold upwelling plumes result in dark areas in SAR images due to an increase in atmospheric stability produced by cooling of the lower atmosphere over the plume. As a consequence of the higher stability, there is a reduction in the amplitude of the capillary waves. Low radar backscatter may also be found at the lee side of topographic obstacles like islands and coastal elevations. Fortunately, these effects do not occur in the study area. In fact, the region is located far from a flat-lying coast, and no islands are present; furthermore, there are no records in the literature of upwelling events in the region. Although biological surfactants are physically and chemically different from seepage slicks, the remote differentiation between these two features is very difficult and sometimes impossible (MacDonald et al., 1993).

The frequent presence of heavy rain cells in tropical regions such as the Amazon River mouth may be the most limiting factor in the use of radar images to detect seepage slicks. In most cases, however, heavy rain cells appear as coarsely rounded shapes (Johannessen et al., 1994), different from natural oil slicks, which in general occur as elongated features.

Study area

The study area is located in the northern portion of the Brazilian equatorial margin in coastal and oceanic waters of Amapá State (**Figure 1**) and covers approximately 83 000 km^2, including the region known as Cone do Amazonas, offshore from the mouth of the Amazon River.

Geological setting

The Foz do Amazonas offshore sedimentary basin is associated with the opening of the South Atlantic Ocean in the Early Cretaceous (Castro et al., 1978). The basin embraces approximately 360 000 km^2, distributed over the continental shelf, slope, and deep waters up to the 3800 m isobath. The basin encompasses different geological subprovinces, which include the Pará and Amapá platforms, the Caciporé half-graben system, a Tertiary carbonate platform, and the Cone do Amazonas deltaic system. The Mesozoic tectonic sedimentary evolution of the region started with the deposition of pre-rift Triassic siliciclastic sediments included in the Calçoene Formation (Brandão and Feijó, 1994) (**Figure 2**). Half-grabens developed as a result of crustal stretching during the rift phase

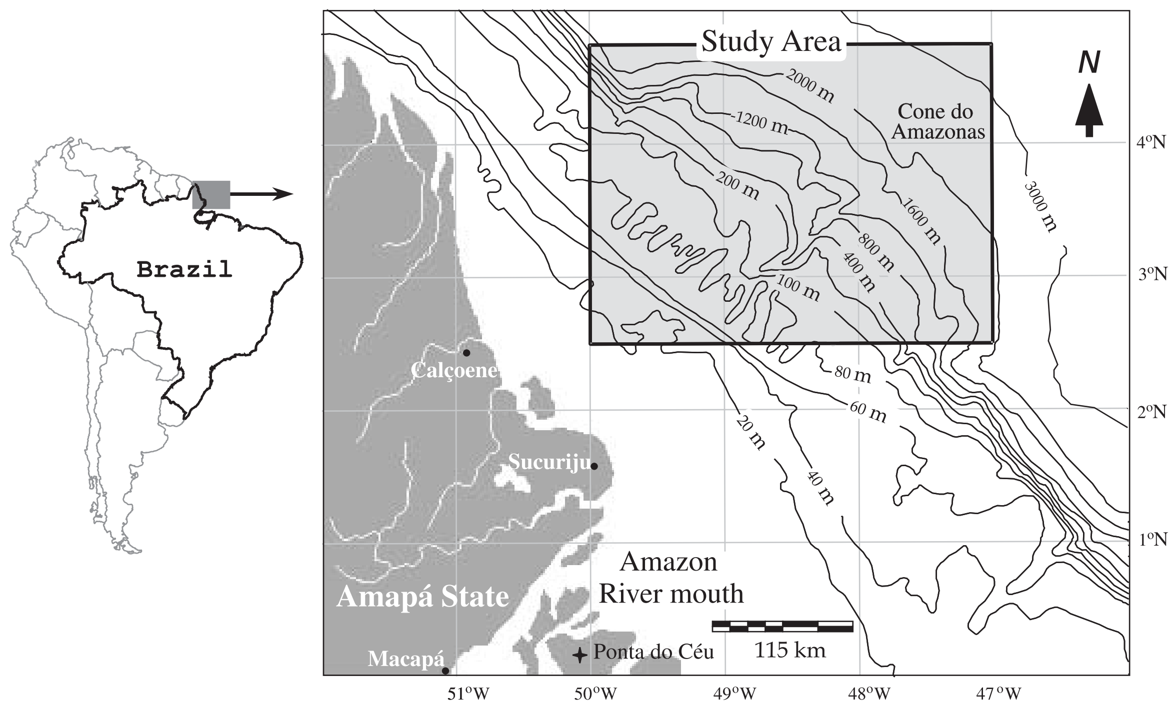

Figure 1. Location map of the study area at the mouth of the Amazon River. Isobath values range from 20 to 3000 m.

contain approximately 6000 m of Aptian–Albian continental to marine shale and intercalated sandstones, included in the Caciporé Formation (Silva and Rodarte, 1989; Silva et al., 1999). The succeeding drift phase began with a dominantly prograding Upper Cretaceous sequence of shale and a sandstone–shale sequence ranging from 2500 to 3000 m in thickness (Limoeiro Formation). A dominantly transgressive Palaeocene – Middle Miocene marine carbonate platform deposited in neritic to bathyal environments (Amapá Formation) was formed overlying the Limoeiro Formation. The youngest sedimentary sequence (Late Miocene – Holocene) is represented by approximately 9000 m of the prograding siliciclastic sequence of the Amazon River delta, comprising the Tucunaré, Pirarucu, and Orange formations (Pará Group).

Interpretation of more than 4500 km of deep-penetration seismic data allowed Silva et al. (1999) to recognize different structural patterns in the Foz do Amazonas Basin. The results obtained by Silva et al. are shown in **Figure 3**, which depicts a schematic geological section in the Cone do Amazonas area (see **Figure 4** for location). The high sedimentation load of the Late Miocene – Holocene sequence created conditions for the development of gravity sliding within an extensional tectonic domain. Such a domain is represented by synsedimentary listric faults and rollover structures near the shelf edge. The kinetic energy of the sliding sediments gave rise seaward to a compressive zone with overthrusting blocks. Over oceanic crust, strike-slip faults with orientation close to east–west are tectonically associated with the St. Paul Fracture Zone.

Figure 4 shows the seismically derived structural map at the top of the Amapá Formation (Miocene) and the isopach map of the Late Miocene – Holocene sequence (Silva et al., 1999). A regularly spaced pattern of listric faults occurs between the shelf edge and the depocentre, whereas thrust faults predominate seaward. The Saint Paul Fracture Zone, with strike-slip faults, marks the transition between continental and oceanic crust.

Petroleum habitat and potential

Main reservoirs in the Foz do Amazonas Basin are clastic rocks of the Caciporé Formation, biocalcarenites of the Amapá Formation (carbonate platform), and Late Miocene – Holocene turbidites of the Pirarucu and Orange formations. Structural and stratigraphic traps were created as a result of gravitational tectonics, which gave rise to listric normal faults over the shelf. Geochemical data indicate that oil in the Amapá and Caciporé formations is correlated with organic extracts from shales of the Caciporé and Limoeiro formations (Mello et al., 2001).

Information about the exploration potential of the Foz do Amazonas Basin for oil and gas is still scarce. Until now, only about 30 wells have been drilled in the area, which corresponds approximately to one well for each 12 000 km^2 (Silva et al., 1999). Based on the presence of a structural pattern represented by growth faults in a giant river-fed submarine fan, however, Mello et al. (2001) recognized potential similarities between the Foz do Amazonas Basin and the Niger Delta Oil Province. The presence of subcommercial shallow water accumulations already identified in the area has indeed confirmed the existence of petroleum systems (as conceived by Magoon and Dow, 1994) in the Foz do Amazonas Basin.

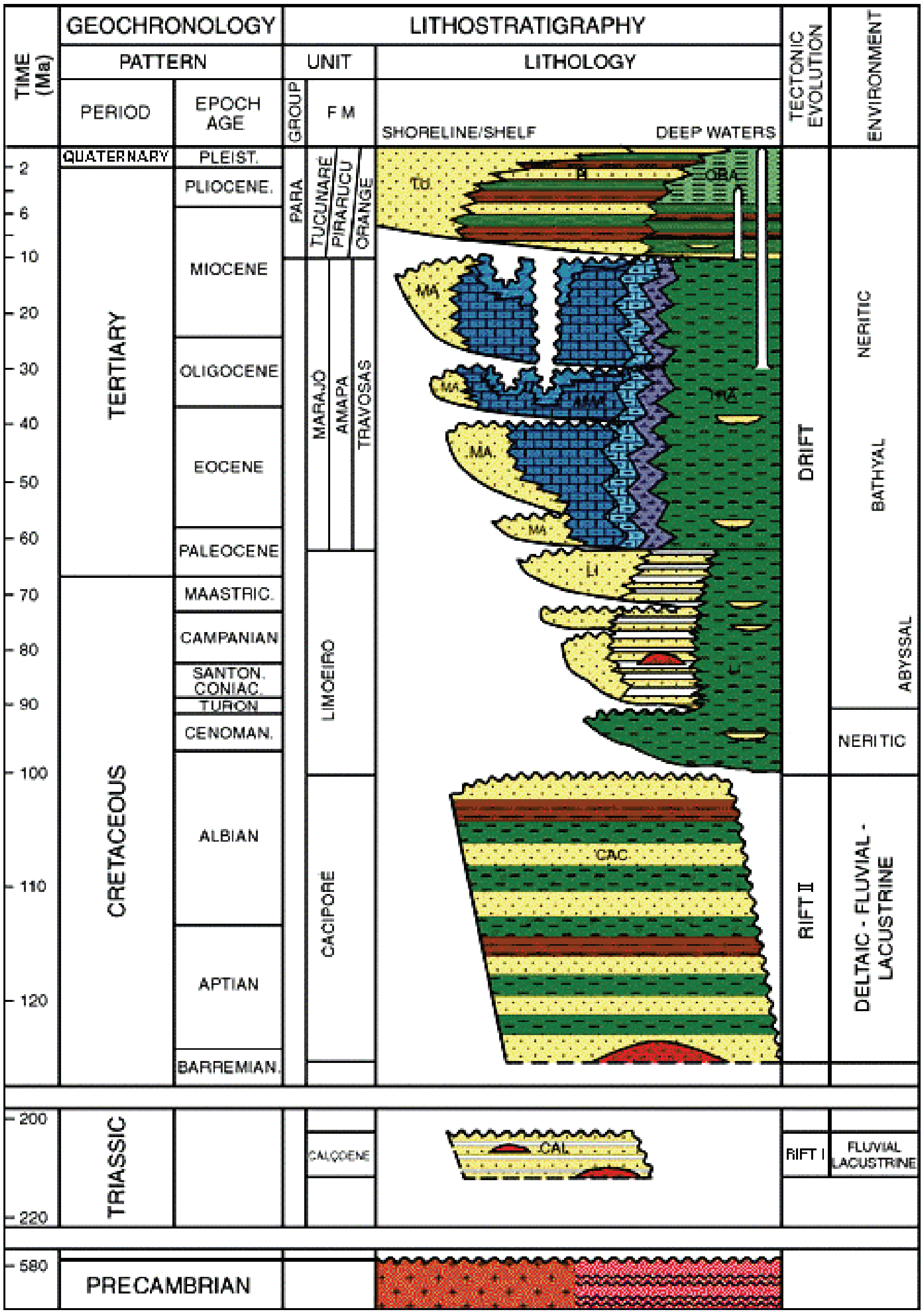

Figure 2. Stratigraphic column of the Foz do Amazonas Basin (Brandão and Feijó, 1994).

Oceanographic features

The study area includes oceanic regions with between 15 and 3000 m of water depth at the mouth of the Amazon River. As the river with the largest flow in the world, the Amazon is responsible for about 15% of freshwater discharge into the oceans (Baumgartner and Reichel, 1975). On average, three million tons of sediments are discharged over the continental shelf per day (Nittrouer et al., 1986). The Amazon River plume of suspended sediments can extend up to 200 km seaward from the river mouth, with a load varying between 80 000 and 250 000 $m^3 \cdot s^{-1}$ (Oltman, 1968). **Figure 5** is a synoptic view of the mouth of the Amazon River, acquired on 3 August 2003 by the moderate-resolution imaging spectroradiometer (MODIS) onboard the Terra platform, and shows the huge plume of suspend sediments discharged into the Atlantic Ocean.

The oceanographic conditions prevailing in the study area include the North Brazil Coastal Current (NBCC) at the outer shelf and slope, with current speeds reaching 1–2 $m \cdot s^{-1}$ (Flagg et al., 1986; Richardson and Reverdin, 1987). Subtidal flow occurs mostly in the northwesterly alongshore direction. With the exception of the salt-wedge front, where the flow has a significant

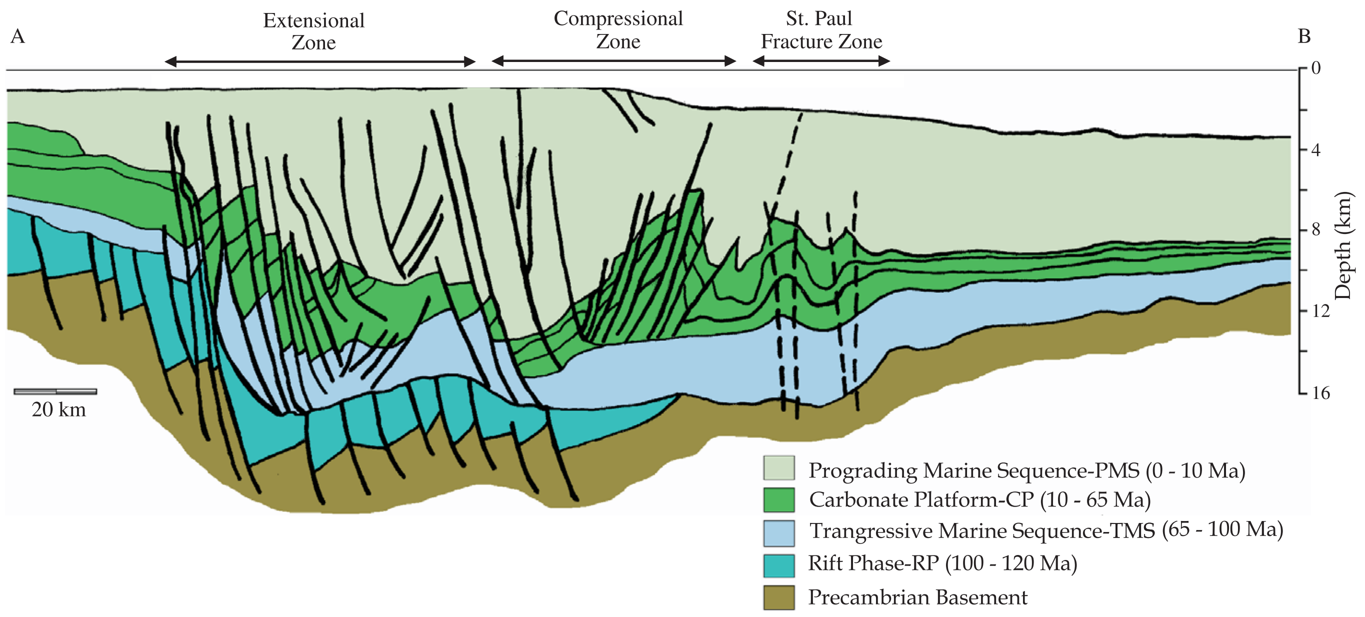

Figure 3. Representative geological section A–B in the central part of the Cone do Amazonas based on multichannel seismic data (modified from Silva et al., 1999). See **Figure 4** for location.

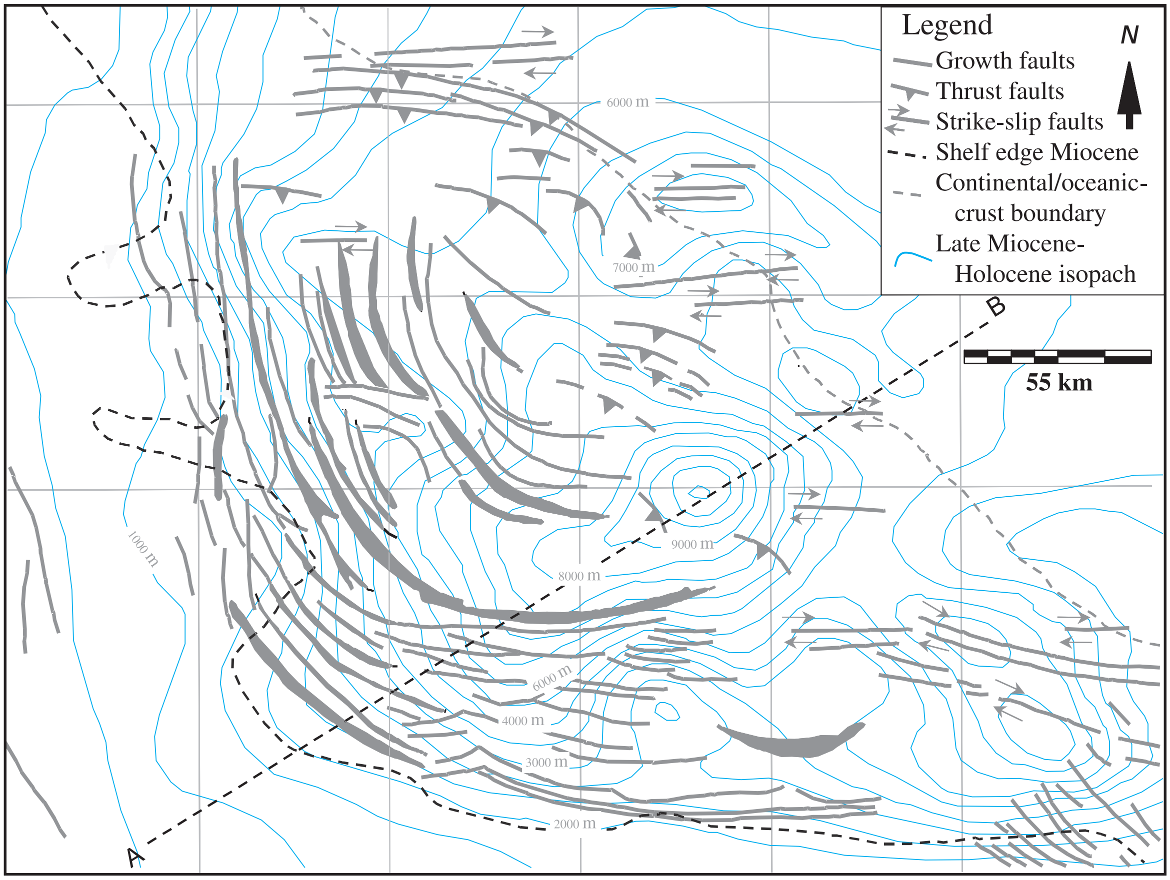

Figure 4. Seismically derived structural map at the top of the Amapá Formation (Miocene), and isopach map of the Late Miocene – Holocene sequence (modified from Silva et al., 1999). Geological section A–B is shown in **Figure 3**.

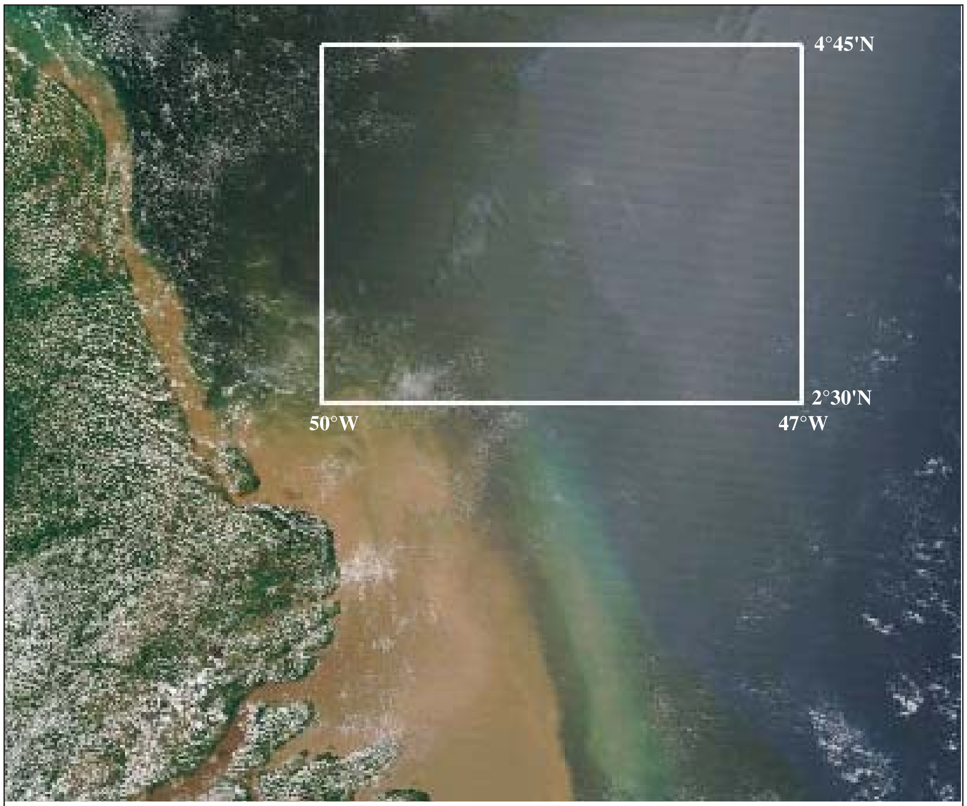

Figure 5. Terra/MODIS colour composite (1R4G3B) acquired on 3 August 2003, showing the large plume of suspended sediment discharged into the Atlantic Ocean by the Amazon River. The box indicates the study area (see **Figure 1** for location).

component in the offshore–onshore direction, elsewhere on the shelf the subtidal flow is relatively strong (~50 cm·s^{-1}) and oriented northwestward (Geyer et al., 1991).

The main tidal component in the Amazon continental shelf is semidiurnal (M2), with amplitudes ranging from 0.70 to 0.85 m at the northern outer shelf. At the northern inner shelf, M2 amplitudes can reach values between 1.50 and 3.00 m, as a result of a resonance mechanism. Large spring–neap and monthly variations are observed in the area. The tidal currents are almost rectilinear and oriented in the cross-isobath direction, with current speeds of 0.5–1.5 m·s^{-1} (Beardsley et al., 1995; Gibbs, 1982). Tidal currents are strongest in the northwest shelf and decrease towards the coast. In front of the river mouth, the tidal behaviour is characteristic of a damped progressive wave. In the northern shelf, the phase difference between elevation and transport is about 60°, or approximately 2 h, increasing to about 90° near the coast, consistent with the behaviour expected of a damped standing wave.

The surface winds in the region are strongly controlled by the position of the Intertropical Convergence Zone (ITCZ). During the austral summer, the ITCZ is in its southernmost position, resulting in northeasterly winds. Conversely, during the austral winter, the ITCZ is in its northernmost position, resulting in east-southeastly winds. Throughout the year, winds are directed mostly onshore, with speeds of 5–10 m·s^{-1}. According to Geyer et al. (1991), a significant part of the along-shelf subtidal current variability over the shelf is correlated with variations in wind stress.

Over the northwest Amazon shelf and slope, one can expect the currents to be a composition of three main forcing mechanisms: (*i*) northeast–southwest rectilinear cross-isobath tidal currents, dominated by the M2 component, with strong spring to neap and monthly variations (0.5–1.5 m·s^{-1}); (*ii*) an alongshore flow over the shelf, mostly in the northwesterly direction and varying between –0.5 and 1.5 m·s^{-1}; and (*iii*) alongshore NBCC flow in the northwesterly direction at the shelf break and slope. Geyer et al. (1991) reported large along-shelf current fluctuations in this region (–0.2–1.3 m·s^{-1}). All these factors were considered in the interpretation of the features identified in the RADARSAT-1 images as associated with seepage slicks.

Geocoded dataset

Different information sources were integrated into a geocoded dataset and included the following.

Previous data — Previous data included (*i*) a seismically derived structural map at the top of the Miocene sequence (Amapá Formation); (*ii*) seismically derived isopach contour maps with a 500 m contour interval of the Palaeocene – Middle Miocene and Late Miocene – Holocene sedimentary sequences (including information from 26 wells); and (*iii*) bathymetric data (contour map and sea-floor-derived digital elevation model).

RADARSAT-1 images — Thirty-eight RADARSAT-1 scenes were analysed in this study (**Table 1**). Descending ScanSAR narrow 1 (SCN1) and wide 1 (W1) beam modes were chosen because of their steep incidence angles (20°–31° for W1 and 20°–40° for SCN1 modes), which make them more sensitive to roughness variations at the ocean surface. Additionally, values of spatial resolutions (30 and 50 m for W1 and SCN1, respectively), with corresponding large area coverage (165 km × 165 km and 300 km × 300 km for W1 and SCN1, respectively), provided a good compromise for seepage slick detection at a regional scale. All the images listed in **Table 1** were submitted to visual analysis with the objective of identifying possible seepage slick candidates. Images containing such features were then selected for unsupervised textural classification and further compared with orbital oceanographic and environmental datasets, with the objective of eliminating false targets.

Complementary information regarding sea surface temperature, cloud top temperature, wind velocity, and tidal regime are essential to support seepage slick interpretation. These oceanographic and environmental datasets must be acquired as close as possible to the time of the RADARSAT-1 image acquisition.

Sea surface temperature and cloud top temperature — Sea surface and cloud top temperatures were obtained from data collected by the thermal infrared bands of the advanced very high resolution radiometer (AVHRR) sensor onboard the TIROS-N series satellite of the National Oceanographic and Atmospheric Administration (NOAA) (**Table 2**). These data were used to identify oceanic features such as fronts, meanders, and eddies and to derive cloud top temperatures. The AVHRR cloud top temperature maps were used to identify regions of high convective activity and possible heavy-precipitation cells. Additionally, to confirm the AVHRR cloud top temperature data, GOES-8 geostationary weather satellite data cloud top temperature maps at 09:00 Greenwich mean time (GMT) and 8 km spatial resolution were also derived, taking advantage of the higher temporal resolution of this orbital system.

Wind speed and direction — The wind vector field for the region was obtained from a 3 day interpolation procedure (Allender, 1977) of the ERS-1/2 scatterometer data. For the low-latitude range of the region, the 1 day scatterometer space coverage results in large data gaps. The steadiness of the wind field at this time scale is sufficiently high to grant an acceptably smooth field. Additionally, wind speed fields were derived from the seven-channel, four-frequency, linearly polarized, passive microwave radiometric data acquired by the Microwave Image (SSM/I) sensor onboard the Defense Meteorological Satellites Program (DMSP) series of satellites. Therefore, wind direction was obtained from the scatterometer ERS-1/2 data, and wind speed, as close as possible to the RADARSAT-1 acquisition time, was derived from the SSM/I radiometer. These data were used to check for the wind threshold limits (3–8 m·s^{-1}) of suitable SAR images for offshore oil detection and to indicate false targets defined by dark, low-wind areas in the images. Although recent work has demonstrated the potential of extracting wind speeds operationally directly from SAR images at subkilometre resolution (Monaldo and Kerbaol, 2004), complications related to the Geophysical Model Function for horizontal transmit, horizontal receive (HH) polarization and a precise radiometric calibration for sigma-zero wide-scan mode RADARSAT-1 images have prevented us from attempting it at this stage.

Table 1. RADARSAT-1 images acquired in the study area (descending orbit).

Scene identification no.	Date of acquisition	Time of acquisition (GMT)[a]	Operational beam mode[b]
C0013814[c]	14 Aug. 1996	09:06:06	W1
M0131161	14 Aug. 1996	09:06:28	W1
C0006757	25 Mar. 1997	09:02:14	SCN1
C0006755	18 Apr. 1997	09:02:07	SCN1
C0007081	18 Apr. 1997	09:02:59	SCN1
C0007084	18 Apr. 1997	09:02:54	SCN1
C0006804[c]	12 May 1997	09:02:12	SCN1
C0006875	29 June 1997	09:02:36	SCN1
C0006808	23 July 1997	09:02:04	SCN1
C0013437	9 Feb. 1999	08:54:56	W1
C0013442	9 Feb. 1999	08:54:33	W1
M0186256	8 Mar. 1999	09:06:15	W1
M0186257	8 Mar. 1999	09:06:38	W1
M0186544	15 Mar. 1999	09:01:59	W1
M0186545	15 Mar. 1999	09:02:22	W1
M0186546	15 Mar. 1999	09:02:45	W1
M0186258	18 Mar. 1999	09:14:32	W1
M0195010	18 Mar. 1999	09:14:44	W1
M0186259	25 Mar. 1999	09:10:20	W1
M0186260	25 Mar. 1999	09:10:43	W1
C0013438	15 Apr. 1999	08:58:00	W1
C0013439	15 Apr. 1999	08:58:23	W1
C0013440	15 Apr. 1999	08:58:46	W1
M0194379	25 Apr. 1999	09:06:19	W1
M0194380	25 Apr. 1999	09:06:42	W1
M0194383	2 May 1999	09:02:55	W1
M0194384	9 May 1999	08:58:11	W1
M0194385	9 May 1999	08:58:34	W1
M0194386	9 May 1999	08:58:56	W1
M0194387	9 June 1999	08:54:29	W1
M0194388	9 June 1999	08:54:52	W1
M0194389	19 June 1999	09:02:13	W1
M0194390	19 June 1999	09:02:37	W1
M0194391	19 June 1999	09:03:00	W1
M0198669	22 June 1999	09:14:36	W1
M0198670	22 June 1999	09:14:59	W1
M0194392	29 June 1999	09:10:30	W1
M0194393[c]	29 June 1999	09:10:53	W1

[a] GMT, Greenwich Meridian Time.

[b] SCN1, ScanSAR narrow 1; W1, wide 1.

[c] Scenes with seepage slick candidates identified by visual analysis and elected for further unsupervised textural classification.

Tidal time series — Hourly time series of tidal sea level elevations at the Ponta do Céu tide gauge (00°05′N, 50°07′W)

Table 2. Acquisition times (GMT) of RADARSAT-1 images with interpreted seepage slicks and orbital remote sensing data used to derive sea surface temperature (AVHRR and GOES-8), cloud top temperature (AVHRR), and wind speed (DMSP–SSM/I).

		Acquisition times of environmental and oceanographic information		
Acquisition date	Acquisition time	Sea surface temperature	Cloud top temperature	Wind speed
14 Aug. 1996	09:06:06	09:45:17	09:00:00	14:06:00
12 May 1997	09:02:12	09:17:54	09:00:00	11:00:00
29 June 1999	09:10:53	07:00:31	09:00:00	08:45:00

were calculated for the months corresponding to the dates of RADARSAT-1 image acquisitions using a harmonic model (Franco, 1988). The model was run using 40 tide constituents provided by the Brazilian Navy Hydrography and Navigation Directorate. Tidal elevations at Ponta do Céu for the three selected RADARSAT-1 images are shown in **Figure 6**. To get the tidal phase at the position of each seepage slick in relation to the tide gauge site we used the M2 component elevation phase map presented by Beardsley et al. (1995) for the whole Amazon shelf. The tidal phase differences between Ponta do Céu and the seepage slicks were converted to hours using the angular speed of 28.9841°/h of the M2 component (**Table 3**). Adding these phase difference hour values to the acquisition of the RADARSAT-1 images in the tidal prediction at Ponta do Céu provided a good estimate of the elevation phase for each seepage slick. The tidal prediction for the region was carried out for two reasons: (*i*) we wanted to see how the monthly variations of the tide between spring and neap phases were affecting the tides during SAR acquisitions; and (*ii*) for each RADARSAT-1 pass, we wanted to know what the tidal elevations should be for the region included in the SAR images and from that try to infer possible tidal current orientation.

Image processing

Preprocessing

The use of digital filters to reduce speckle noise was the first step in the image processing. Several adaptive and nonadaptive despeckling filters were tested. The best results, in terms of minimum loss of textural information and preserving edges, were obtained with a 3 × 3 window Frost filter. Images were then processed in full spatial and radiometric resolution (16 bits) and georeferenced on the basis of the satellite ephemeris data using a second-degree polynomial rectification algorithm (root-mean error of 0.8) with bilinear interpolation. When compared with identified onshore features, absolute position errors in the corrected scenes were no greater than 100 m. Lastly, image classification was carried out using rescaled eight-bit data.

Textural classification

Seepage slicks are smooth at C-band RADARSAT-1 data and therefore produce mostly specular reflection away from the SAR antenna, resulting in very low digital numbers (DN). The

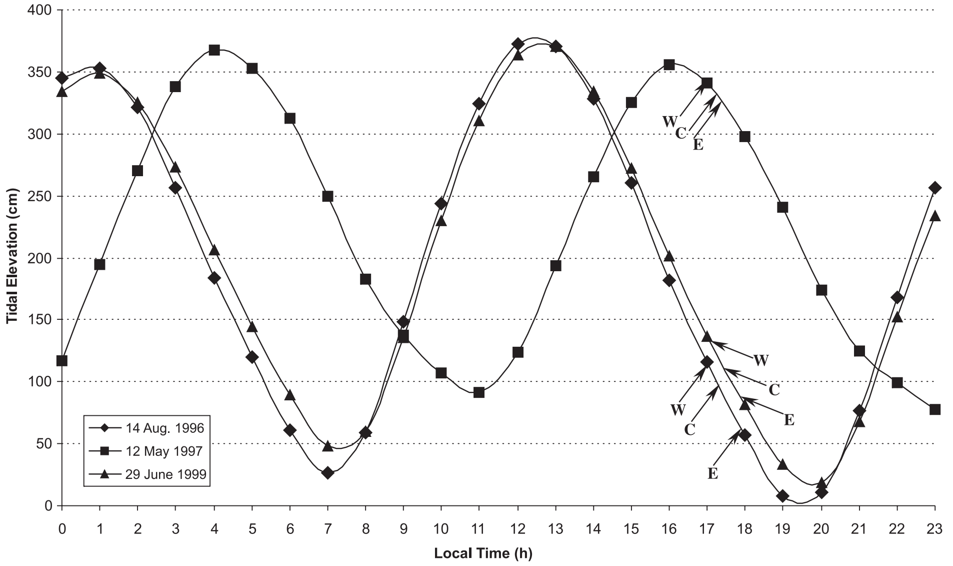

Figure 6. Time series of tidal elevation relative to the Ponta do Céu tide gauge (see **Figure 1** for location). Letters W, E, and C refer to calculated tidal conditions for the upper left corner, lower right corner, and centre of each RADARSAT-1 scene, respectively.

Table 3. Forecasted tidal elevation at the Ponta do Céu tide gauge site.

Date	High water (cm)	Low water (cm)	Tidal range (cm)	Maximum range of spring tide (%)
14 Aug. 1996	372	8	364	81
12 May 1997	356	78	278	62
29 June 1999	371	19	352	79

digital image processing to enhance areas of smooth texture was based on an unsupervised semivariogram textural classifier algorithm. The semivariogram function describes how the spatial continuity of a regionalized variable changes with the distance and direction, given by Isaaks and Srivastava (1989) as follows:

$$\hat{\gamma}(\boldsymbol{h}) = \frac{1}{2N(\boldsymbol{h})}\sum_{i=1}^{N}[z(\boldsymbol{x}_i) - z(\boldsymbol{x}_i + \boldsymbol{h})]^2,$$

where $\hat{\gamma}(\boldsymbol{h})$ is the semivariogram estimator, $z(\boldsymbol{x}_i)$ is the value of the regionalized variable at location $\boldsymbol{x}_i$, $z(\boldsymbol{x}_i + \boldsymbol{h})$ is the value of the regionalized variable at a location $\boldsymbol{h}$ away from $\boldsymbol{x}_i$, and $N(\boldsymbol{h})$ is the number of pairs being compared at lag distance $\boldsymbol{h}$.

The ideal shape of a semivariogram has a value of zero for $\boldsymbol{h} = 0$, rising smoothly upwards as $\boldsymbol{h}$ increases, until a value of $\boldsymbol{h}$ is reached at which $\hat{\gamma}(\boldsymbol{h})$ no longer increases and curves into a straight horizontal line, meaning that the regionalized variable reached a completely random behaviour. This semivariogram shape is referred to as spherical [$\hat{\gamma}(\boldsymbol{h}) = C_0 + C_1\ \mathrm{Sph}(\boldsymbol{h}/a)$]. Range a, contribution C_1, and nugget effect C_0 are important features of a spherical semivariogram. The range is the lag distance at which $\hat{\gamma}(\boldsymbol{h})$ reaches a plateau, the sill C, and no longer increases. The sill is typically equal to the variance of the dataset. The nugget effect is a discontinuity at the origin of the semivariogram that jumps to intersect the vertical axis at a value greater than zero.

Each random spatial phenomenon is unique, having a unique semivariogram. Depending on the nature of the phenomenon, and mostly on how it is sampled, the corresponding semivariogram may or may not display a nugget. A relatively large nugget effect indicates short-scale variability of the dataset, or a rather high level of randomness. Two different targets display semivariograms with different statistical parameters. In this study, an isotropic (no directional information) semivariogram function was used, which can be considered as an average of the various directional semivariograms. To avoid contamination, small training masks of 12 pixels × 12 pixels were defined for the calculation of the semivariogram values for both seepage slicks and neighbouring sea clutter. After this, separation distances were grouped into their integer parts (e.g., a separation distance of 3.7 was considered as 3). Results indicated that seepage slicks have a distinctive semivariogram, hence a unique statistical fingerprint compared with neighbouring sea clutter areas (**Figure 7**; **Table 4**).

The seepage slick semivariogram presents spherical behaviour, with a wing range value of 120 m (4 pixels) and sill value of 27. A small discontinuity at the origin of the semivariogram (nugget effect) is also observed. Because seepage slicks are related to specular reflection at C-band RADARSAT-1 data, the radar beam is reflected away from the antenna. Such a condition gives rise to a SAR dataset with decreased spatial structure and limited DN variability (**Figure 7a**).

The semivariogram for sea clutter also presents spherical behaviour, with an increased range of 210 m (7 pixels) and sill value of 4300. The pronounced nugget effect is possibly indicative of increased spatial randomness within the chosen RADARSAT-1 W1 sample for such a cover type. In this case, the incident radar beam is diffusely backscattered by the rough sea surface. As a result, a stronger signal is received by the antenna, giving rise to a SAR dataset in which the spatial structure is more developed (**Figure 7b**).

Differences in semivariogram behaviour as described previously demonstrate that textural classification of RADARSAT-1 data for seepage slick detection is a feasible task. In this study, the chosen algorithm was the unsupervised semivariogram textural classifier (USTC). It is a deterministic classifier, which provides the option of combining both textural and radiometric information (Miranda et al., 1997). Radiometric information is conveyed by the despeckled digital number ($\mathrm{DN_{dsp}}$) value. Textural information is described by the shape and value of the circular semivariogram function, which has the following form:

$$\gamma(\boldsymbol{x}_0, \boldsymbol{r}) = \frac{1}{2n}\sum_{\theta=0}^{2\pi}[\mathrm{DN}(\boldsymbol{x}_0 + r) - \mu_H(\boldsymbol{x}_0)],$$

where $\gamma(\boldsymbol{x}_0, \boldsymbol{r})$ is the semivariogram function at pixel location $\boldsymbol{x}_0$ and radial lag distance of $\boldsymbol{r}$ pixels, $\mathrm{DN}(\boldsymbol{x}_0 + r)$ is the digital number value at radial lag distance $\boldsymbol{r}$ from $\boldsymbol{x}_0$ (radius $\boldsymbol{r}$, angle θ), $\mu_H(\boldsymbol{x}_0)$ is the mean value of a circular neighbourhood of radius H, centre $\boldsymbol{x}_0$, H is the maximum radial lag distance (in pixels) suitable to describe the data (the range a), and n is the number of pixel neighbours at radial lag distance $\boldsymbol{r}$.

Textural information is also described by the digital number variance in a circular neighbourhood of radius H around the pixel $\boldsymbol{x}_0$ ($\sigma_H^2(\boldsymbol{x}_0)$). The DN variance is included in the classification procedure because it reflects the value of the semivariogram function for a very large lag distance (greater than H).

For a pixel location $\boldsymbol{x}_0$ in a RADARSAT-1 image, the vector $\boldsymbol{Z}(\boldsymbol{x}_0)$ of dimension $H + 2$ has the following form:

$$\boldsymbol{Z}(\boldsymbol{x}_0) = [\mathrm{DN_{dsp}}(\boldsymbol{x}_0), \gamma(\boldsymbol{x}_0,1), \gamma(\boldsymbol{x}_0,2), \ldots, \gamma(\boldsymbol{x}_0, H), \sigma_H^2(\boldsymbol{x}_0)].$$

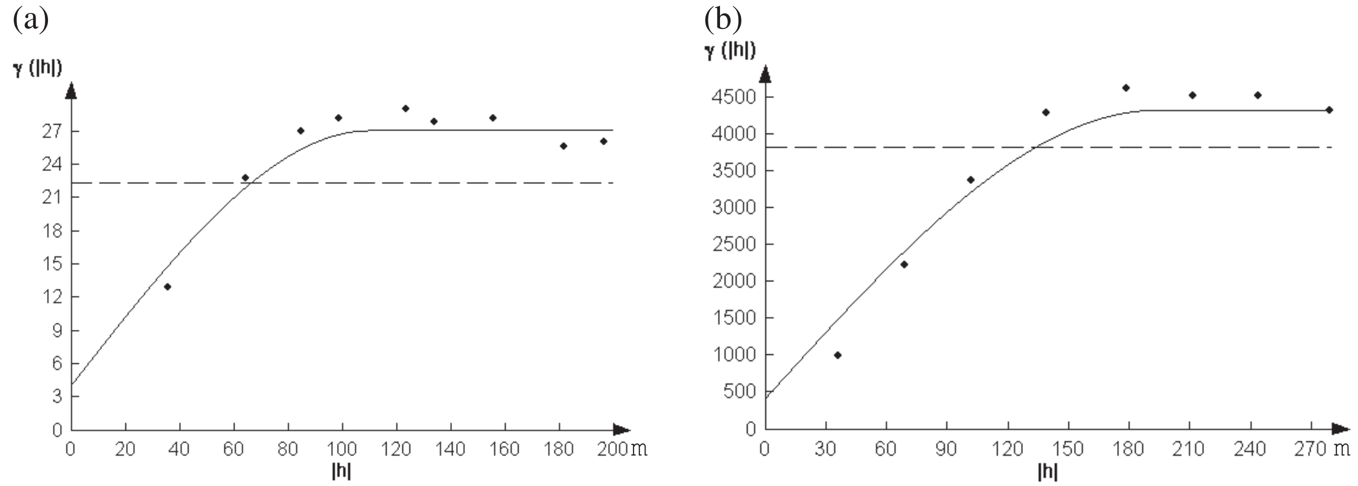

Figure 7. Isotropic semivariograms for areas of (a) seepage slicks and (b) sea clutter, as portrayed in the RADARSAT-1 W1 image acquired on 14 August 1996. Sample size is 12 pixels × 12 pixels.

Table 4. Statistical characteristics of the RADARSAT-1 samples (eight-bit digital number, 12 pixels × 12 pixels) used for the semivariogram calculations.

Cover type	Mean	Median	Min.	Max.	Variance
Seepage slicks	2	0	0	22	23
Sea clutter	151	162	15	255	3842

The classification procedure is accomplished based on all components of this $H + 2$ dimensional vector calculated for each pixel location. The ISODATA clustering algorithm is applied to carry out the unsupervised classification of this set of vectors. After the unsupervised classification, results obtained from the clustering program are merged together through interactive class aggregation (an aggregate is a grouping of one or more classes considered to be of thematic significance). In this study, class aggregation was performed to discriminate patches of smooth texture from rough to intermediate offshore areas of the RADARSAT-1 image. Raster polygons defining smooth surface regions related to seepage slicks were converted to the vector format (**Figure 8**).

Results and discussions

As a result of the USTC algorithm application, several regions with smooth texture were identified in the RADARSAT-1 images. After elimination of false targets by using the ancillary oceanographic and meteorological information, distinctive elongated features were interpreted as associated with seepage slicks. Only three of the 38 analysed RADARSAT-1 scenes (**Table 1**) presented features interpreted as seepage slicks (**Figure 9**): six occur in the scene acquired on 14 August 1996, 11 in the scene acquired on 12 May 1997, and four in the scene acquired on 29 June 1999. They range in surface area from 0.042 to 35.657 km^2, with a mean of 5.464 km^2 (standard deviation ± 8.153 km^2).

All features interpreted as associated with seepage slicks occur over continental crust, mostly in water depths of less than 100 m (**Table 5**). Interpreted seepage slicks were analysed taking into account the tidal regime at the time of the RADARSAT-1 acquisition and the characteristic dynamical setting of subtidal currents expected in the region, as described in the technical literature (e.g., Geyer et al., 1991). Thus, seepage slicks interpreted in the images acquired on 14 August 1996 and 29 June 1999 were associated with a relatively strong amplitude tidal signal of about 81% of the maximum range of spring tides (**Table 3**). On the other hand, seepage slicks interpreted in the image from 12 May 1997 were under a weaker tidal signal, with the minimum neap tidal range observed 3 days later (**Table 3**).

Most of the interpreted seepage slicks are oriented either east–west or northwest–southeast. Features with a northwest–southeast direction may result from the Along Shore Coastal Current (ACC) or from the North Brazil Coastal Current (NBCC) at shelf break. In addition, east–west-oriented seepage slicks seem to be the vector result of the southeast–northwest along-shelf flow with a northeast–southwest cross-isobath tidal flow. The spatial outline of seepage slicks 3 and 8 presents two distinct orientations (**Figure 8**), probably due to changing oceanographic and (or) meteorological forcings during seepage history. Despite their orientation, those features are located over the slope in deeper waters, mostly under the influence of the NBCC. **Table 5** summarizes the main characteristics of the interpreted seepage slicks, the tidal regime at the time of the

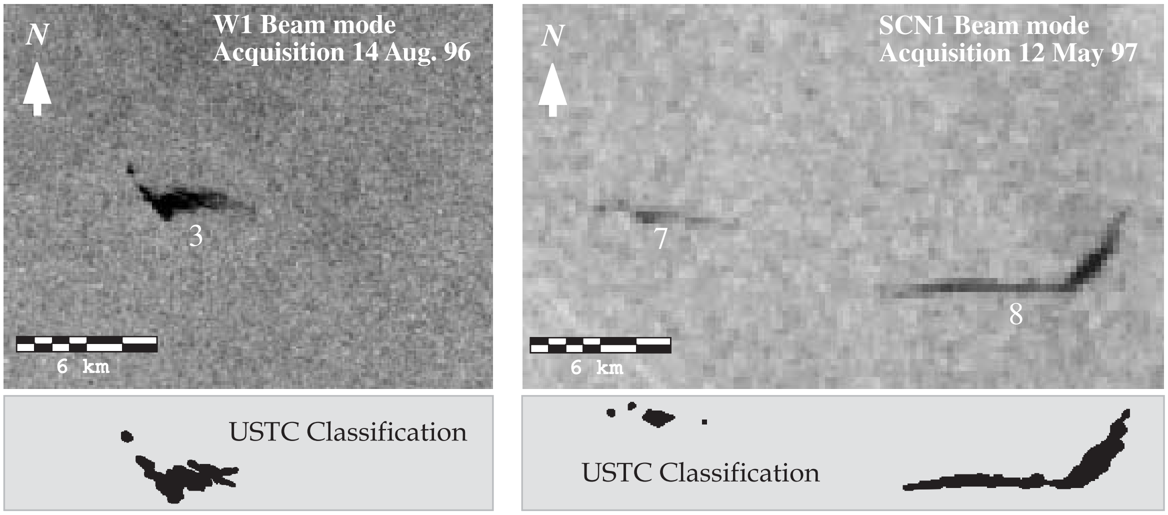

Figure 8. Examples of seepage slicks identified on RADARSAT-1 SCN1 and W1 images and corresponding USTC classification results. Numbers refer to seepage slick identification numbers in **Table 5**.

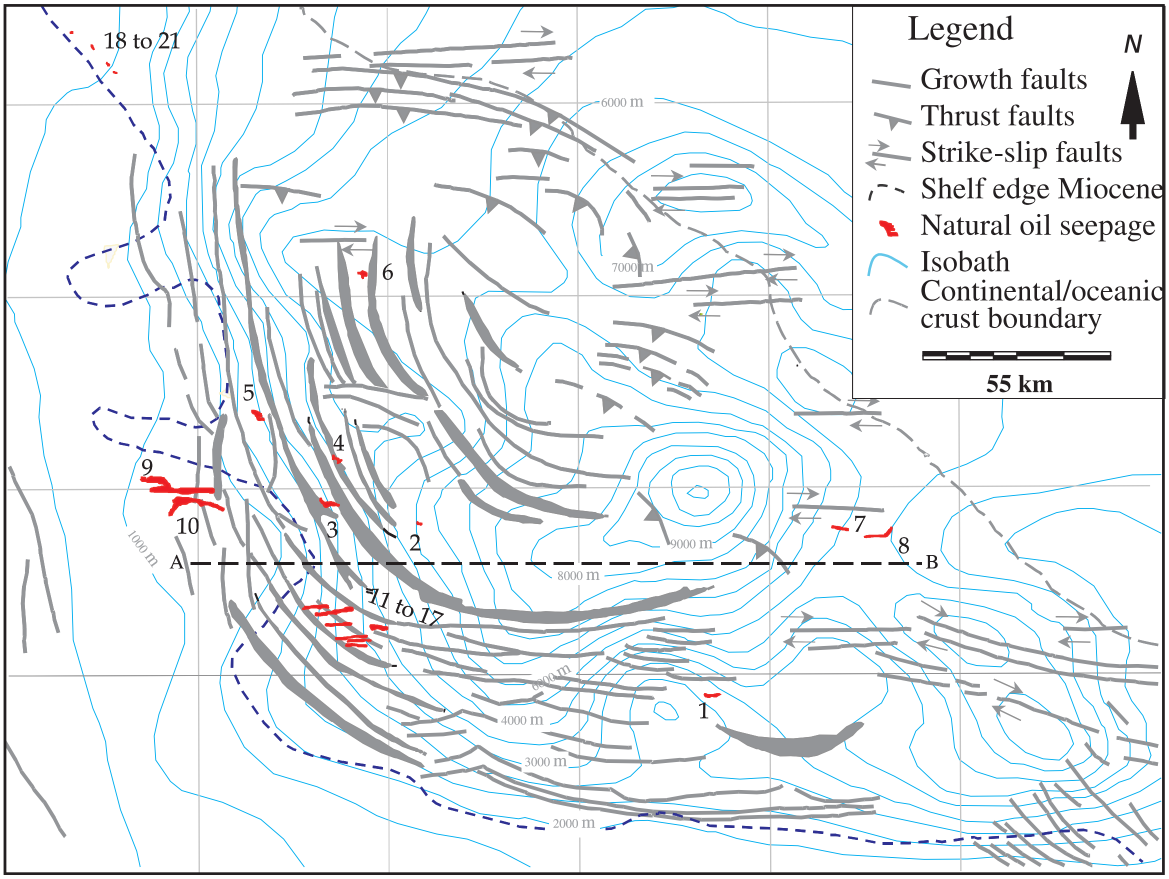

Figure 9. Interpreted seepage slicks 1–21 overlayed on the seismically derived structural map at the top of the Amapá Formation (Miocene), and isopach map of the Late Miocene – Holocene sequence (modified from Silva et al., 1999). Idealized cross section A–B is shown in the tectonic model of **Figure 10**.

RADARSAT-1 acquisition, and prevailing meteorological conditions at the time of the satellite passage.

Figure 9 shows the spatial distribution of the interpreted seepage slicks in the study area. Since oil slicks are floating over the sea surface, a key point for spatial pattern reasoning is to infer how far (lateral displacement) they are from their source areas at the sea floor. In the Gulf of Mexico, MacDonald et al. (1993) reported that lateral displacements have been less

Table 5. Characteristics of interpreted seepage slicks with oceanographic and meteorological conditions prevailing close to the time of acquisition of the RADARSAT-1 images.

Seepage slick	Tectonic domain	RADARSAT -1 acquisition date	Seepage slicks characteristics			Oceanographic conditions		Meteorological conditions		
			Area (km^2)	Water depth (m)	Predominant orientation	Phase lead to Ponta do Céu (h)	Currents[a]	Proximity of rain cells	Sea surface temp. (^{o}C)	Wind conditions
1	Extensional zone	14 Aug. 1996	2.818	~200	E–W	7.3	HT+NBCC	No	24.5–25.6	~3.5 m·s^{-1} South–south-west
2			0.611	~110	NW–SE; E–W		HT+ACC			
3			5.171	~75						
4			1.701	~95	NW–SE					
5			4.203	~90						
6			2.680	~650	E–W	7.50	HT+NBCC			
7	Compressional zone	12 May 1997	2.447	~1200			F+NBCC		22.5–24.0	~4.5 m·s^{-1} West–south-west
8			4.380		E–W; NE–SW			Yes		
9	Extensional zone		35.657	~80	E–W	7.14	F+ACC			
10			20.290					No		
11			4.530							
12			8.826							
13			4.723			6.80				
14			5.025			6.90				
15			4.424							
16			2.939			6.80				
17			3.348			6.55				
18	No structural information available	29 June 1999	0.220	~2100	NW–SE	7.60	NBCC		23.0–24.0	~5.5 m·s^{-1} West
19			0.363							
20			0.359							
21			0.042							

[a] HT, high tide; F, flooding tide; ACC, along-shore coastal current; NBCC, North Brazil Coastal Current.

than 0.5 km in water depths ranging from 500 to 2000 m. Due to the effects of evaporation and weathering, MacDonald et al. also found that plumes of oil with lengths of about 5 km last less than 1 day after reaching the sea surface. Additionally, Fallah and Stark (1976) showed that the advection of an oil spill produced exclusively by the wind is only 3%–4% of the wind speed.

In our study, with a calculated mean wind speed of 4.5 $m\cdot s^{-1}$ during the acquisition of the RADARSAT-1 images, the expected drift of a seep produced exclusively by the wind is estimated to be around 13.6 km per day. On the other hand, the advection of a seepage slick under tidal dominance is expected to have back and forth behaviour. During the first half of the tidal period (about 6 h in the region) the slick would be advected in one direction, whereas in the following 6 h period it would be advected in the opposite direction, with only a reduced net drift. Thus, considering that most of the interpreted seeps in the study area occur along the shelf in water depths less than 100 m, out of the influence of the NBCC, it is reasonable to infer that they are not far from their original sources at the sea floor.

Taking this information into account, comparison of the seepage slicks with the structural map at the top of the Amapá Formation (Miocene) showed that 15 of the interpreted seepage slicks, i.e., approximately 71% of the total number of interpreted seepage slicks, occur in the extensional tectonic domain in an area with a predominance of listric normal faults (**Table 5**; **Figure 9**). Exceptions are seepage slicks 7 and 8, which occur associated with east–west strike-slip faults in the compressional tectonic domain, not far from the boundary between continental and oceanic crust. Seepage slicks 18–21 occur in the northwesternmost part of the study area, a region devoid of structural information.

The analysis of 38 RADARSAT-1 images over a period of 3 years indicated no areas with continuous-seepage slicks. The interpreted oil slicks are tentatively associated with episodic releases of oil as a result of Cenozoic gravity tectonics pushed by the overpressure of a huge pile of sediments transported by the Amazon River since the Late Miocene (Franke, 1975).

Based on seismic data, Silva and Rodarte (1989) and Silva et al. (1999) proposed a tectonic model for the Cone do Amazonas area as a response to the expressive sedimentary load in the continental slope. According to this model, gravity sliding created an extensional zone on the continental slope, with the development of growth faults and rollover structures. The kinetic energy of the sliding mass of Cenozoic sediments was enough to allow tectonic transportation towards deep water, giving rise to a compressive zone due to the stacking of the overthrusting block. Analogous models have been proposed for other deltaic areas such as the Gulf Coast Province and Niger delta (Crans et al., 1980; Galloway, 1986).

Figure 10 is a sketch of the gravity-sliding model for the study area. This model explains the episodic occurrence of oil seepage as a result of pressure alleviation mainly in the extensional zone along growth faults, which are inherent structural features associated with this stress regime of prograding siliciclastic delta sequences. It is well known that such features are responsible for creating hydrocarbon traps and for constituting critical avenues for fluid circulation within the sedimentary sequence.

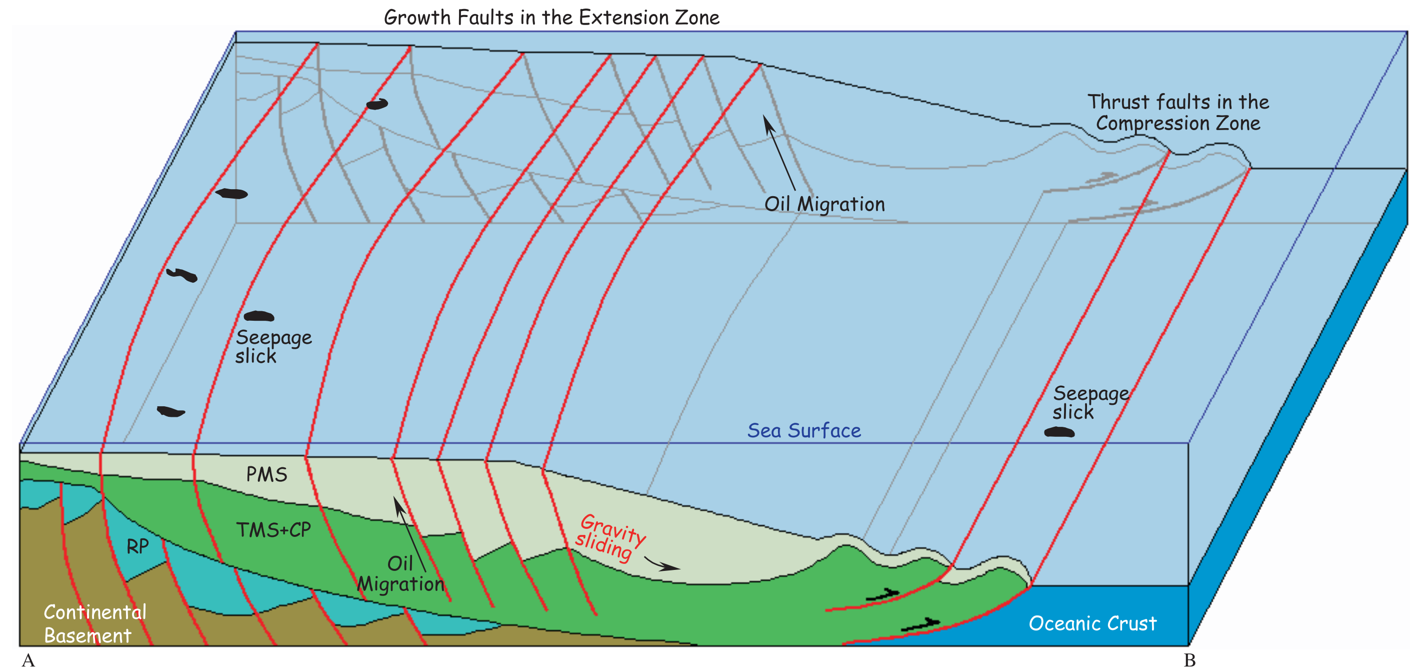

Figure 10. Gravity sliding tectonic model to explain the distribution of seepage slicks in the Foz do Amazonas Basin. PMS, prograding marine sequence; RP, rift phase; TMS + CP, transgressive marine sequence + marine carbonate platform. See **Figure 3**.

Conclusions

The analysis of the RADARSAT-1 images using the SCN1 and W1 beam modes allowed the definition of distinct areas of smooth textural features that were interpreted as seepage slicks in the Foz do Amazonas Basin. Spatial correspondence of interpreted oil slicks with geological structures seismically mapped at the top of the Amapá Formation (Miocene) suggests the control of gravitational tectonics on oil seepage. Most of the seepage slicks occur in the extensional tectonic domain associated with growth faults. Together with previously discovered subcommercial shallow water oil accumulations by Petrobras, the remote detection of seepage slicks is additional evidence of the exploration potential of the area.

Considering the high costs of offshore exploration, information derived from radar remote sensing coupled with multisource data may contribute significantly to minimize risks in offshore frontier areas such as the Foz do Amazonas Basin.

Acknowledgments

This research was carried out under the CTPETRO-1 Program, with financial support from Petrobras and FINEP/FNDCT. The first author was also supported by a grant from the Conselho Nacional de Desenvolvimento Científico e Tecnológico (CNPq).

References

Allender, A.H. 1977. Comparison of model and observed currents in Lake Michigan. *Journal of Physical Oceanography*, Vol. 7, pp. 711–718.

Alpers, W., and Hühnerfuss, H. 1989. The dumping of ocean waves by surface films: a new look at an old problem. *Journal Geophysical Research*, Vol. 94, No. C5, pp. 6251–6265.

Baumgartner, A., and Reichel, E. 1975. *The world water balance*. Elsevier, New York. 179 pp.

Beardsley, R.C., Candela, J., Limeburner, R., Geyer, W.R., Lentz,. S.J., Castro, B.M., Cacchione, D., and Carneiro, N. 1995. The M_2 tide on the Amazon shelf. *Journal of Geophysical Research*, Vol. 100, No. C2, pp. 2283–2319.

Brandão, J.A.S., and Feijó, F.J. 1994. Bacia da Foz do Amazonas. *Boletim de Geociências da PETROBRAS*, Vol. 8, pp. 91–99.

Castro, J.C., Miura, K., and Braga, J.A.E. 1978. Stratigraphic and structural framework of the Foz do Amazonas basin. In *Proceedings of the 10th Annual Offshore Technology Conference*, 8–11 May 1978, Houston, Tex. Society of Petroleum Engineers, Houston, Tex. Vol. 1, pp. 1843–1847.

Crans, W., Mandl, G., and Haremboure, J. 1980. On the theory of growth faulting: a geomechanical delta model based on gravity sliding. *Journal of Petroleum Geology*, Vol. 2, pp. 265–307.

Estes, J.E., Crippen, R.E., and Star, J.L. 1985. Natural oil seep detection in the Santa Barbara Channel, California, with shuttle imaging radar. *Geology*, Vol. 13, pp. 282–284.

Fallah, M.H., and Stark, R.M. 1976. Literature review: movement of spilled oil at sea. *Marine Technology Society Journal*, Vol. 10, pp. 3–18.

Fingas, M., and Brown, C. 1997. Remote sensing of oil spill. *Sea Technology*, Vol. 38, pp. 37–46.

Flagg, C.N., Gordon, R.L., and McDowell, S. 1986. Hydrographic and current observations on the continental slope and shelf in the Western Equatorial Atlantic. *Journal of Physical Oceanography*, Vol. 16, pp. 1412–1429.

Franco, A.S. 1988. *Tides fundamentals, analysis and prediction*. Fundação Centro Tecnológico de Hidráulica, São Paulo, Brazil. Internal Report, 249 pp.

Franke, M.R. 1975. Pressões de formação anormalmente altas. *Boletim Técnico da Petrobras*, Vol. 18, pp. 56–66.

Galloway, W.E. 1986. Growth faults and fault-related structures of prograding terrigenous clastics continental margins. *Transactions of the Gulf-Coast Association of Geological Societies*, Vol. 36, pp. 121–128.

Geyer, W.R., Beardsley, R.C., Candela, J., Castro, B.M., Legeckis, R.V., Lentz, S.J., Limeburner, R., Miranda, L.B., and Trowbridge, J.H. 1991. The physical oceanography of the Amazon outflow. *Oceanography*, Vol. 4, pp. 8–14.

Gibbs, R.J. 1982. Currents on the shelf of northeastern South America. *Estuarine, Coastal and Shelf Science*, Vol. 14, pp. 283–299.

Isaaks, E.H., and Srivastava, R.M. 1989. *An introduction to applied geostatistics*. Oxford University Press, New York. 560 pp.

Johannessen, J.A., Digranes, G., Espedal, H., Johannessen, O.M., Samuel, P., Browne, D., and Vachon, P. 1994. *SAR ocean feature catalogue*. ESA Publications Division, c/o ESTEC, Noordwijk, The Netherlands. ESA SP-1174. 106 pp.

MacDonald, I.R., Guinasso, N.L., Jr., Ackleson, S.G., Amos, J.F., Duckworth, R., and Brooks, J.M. 1993. Natural oil slicks in the Gulf of Mexico visible from space. *Journal of Geophysical Research*, Vol. 98, No. C9, pp. 16 361 – 16 364.

MacDonald, I.R., Reilly, J.F., Jr., Best, S.E., Venkataramaiah, R., Sassen, R., Guinasso, N.L., Jr., and Amos, J.F. 1996. Remote sensing inventory of active oil seeps and chemosynthetic communities in the northern Gulf of Mexico. In *Hydrocarbon migration and its near-surface expression*. Edited by D. Schumacher and M.A. Abrams. American Association of Petroleum Geologists, Memoir 66, Chapt. 3, pp. 27–37.

Magoon, L.B., and Dow, W.G. 1994. The petroleum systems. In *The petroleum systems: from the source to trap*. Edited by L.B. Magoon and W.G. Dow. American Association of Petroleum Geologists, Memoir 60, pp. 3–24.

Mello, M.R., Mosmann, R., Silva, S.R.P., Maciel, R.R., and Miranda, F.P. 2001. Foz do Amazonas area: the last frontier for elephant hydrocarbon accumulations in the South Atlantic realm. In *Petroleum provinces of the twenty-first century*. Edited by M.W. Downey, J.C. Threet, and W.A. Morgan. American Association of Petroleum Geologists, Memoir 74, Chapt. 20, pp. 403–414.

Miranda, F.P., Fonseca, L.E.N., Beisl, C.H., Rosenqvist, A., and Figueiredo, M.D.M.A.M. 1997. Seasonal mapping of flooding extent in the vicinity of the Balbina Dam (Central Amazônia) using RADARSAT-1 and JERS-1 SAR data. In *Proceedings of the International Symposium on Geomatics in the Era of RADARSAT* (GER'97), 26–30 May 1997, Ottawa, Ont. Natural Resources Canada, Ottawa, Ont. CD-ROM.

Miranda, F.P., Bentz, C.M., Beisl, C.H., Lorenzzetti, J.A., Araújo, C.E.S., and Silva, C.L., Jr. 1998. Application of unsupervised semivariogram textural classification of RADARSAT-1 data for the detection of natural oil seeps offshore the Amazon River mouth. In *RADARSAT ADRO Symposium*, 13–15 September 1998, Montréal, Que. CD-ROM. Canadian Space Agency, St. Hubert, Que. 10 pp.

Miranda, F.P., Marmol, A.M.Q., Pedroso, E.C., Beisl, C.H., Welgan, P., and Morales, L.M. 2004. Analysis of RADARSAT-1 data for offshore monitoring activities in the Cantarell Complex, Gulf of Mexico, using the unsupervised semivariogram textural classifier (USTC). *Canadian Journal of Remote Sensing*, Vol. 30, No. 3, pp. 424–436.

Monaldo, F., and Kerbaol, V. 2004. The SAR measurement of ocean surface winds: an overview. In *Proceedings of the 2nd Workshop on Coastal and Marine Applications of SAR*, 8–12 September 2003, Svalbard, Norway. ESA Publications Division, c/o ESTEC, Noordwijk, The Netherlands. ESA SP-565. pp. 15–32.

Nittrouer, C.A., Curtin, T.B., and DeMaster, D.J. 1986. Concentration and flux of suspended sediment on the Amazon continental shelf. *Continental Shelf Research*, Vol. 6, pp. 151–174.

Oltman, R.E. 1968. *Reconnaissance investigation of the discharge and water quality of the Amazon River.* US Geological Survey, Circular 552. 16 pp.

Richardson, P.L., and Reverdin, G. 1987. Seasonal cycle of velocity in the Atlantic North Equatorial Undercurrent as measured by surface drifters, current meters, and shipdrifts. *Journal of Geophysical Research*, Vol. 92, pp. 3691–3708.

Silva, S.R.P., and Rodarte, J.B.M. 1989. Bacias da Foz do Amazonas e Pará-Maranhão (águas profundas): uma análise sismoestratigráfica, tectono-sedimentar e térmica. In *Proceedings of the 1st Congress of the Brazilian Geophysical Society*, 20–24 November 1989, Rio de Janeiro, Brazil. Brazilian Geophysical Society, Rio de Janeiro. Vol. 2, pp. 843–852.

Silva, S.R.P., Maciel, R.R., and Severino, M.C.G. 1999. Cenozoic tectonics of Amazon Mouth Basin. *Geo-Marine Letters*, Vol. 18, pp. 256–262.

Stankiewicz, B.A. 2003. Integration of geoscience and engineering in the oil industry — just a dream? *Nature (London)*, Vol. 426, pp. 360–363.

Staples, G.C., and Hodgins, D.O. 1998. RADARSAT-1 emergency response for oil spill monitoring. In *Proceedings of the 5th International Conference on Remote Sensing for Marine and Coastal Environments*, 5–7 October 1998, San Diego, Calif. Edited by B. Petosky. ERIM International Inc., Ann Arbor, Mich. pp. 1–5e.

White, N., Thompson, M., and Barwise, T. 2003. Understanding the thermal evolution of deep-water continental margins. *Nature (London)*, Vol. 426, pp. 334–343.

Wilson, R.R., Managhan, P.H., Osanick, A., Price, L.C., and Rogers, M.A. 1974. Natural marine oil seepage. *Science (Washington, D.C.)*, Vol. 184, pp. 857–865.